

**AKAY/HANDBOOK OF NEURAL ENGINEERING  
INSTRUCTIONS FOR CONTRIBUTORS  
HANDLING PAGE PROOFS**

A pdf file of each chapter is being emailed to the author identified as the contact author on a list supplied by Professor Akay. Please handle the materials in the following manner:

1. Print a set of proof. Proofread the pages, answers all queries and the query sheet provided with the proofs and make whatever corrections are necessary, including illustration corrections. If you replace an illustration or illustrations are marked FPO, please email a new version and fax a hardcopy of that file with your proof corrections.
2. When making the corrections, please note, next to the correction, any errors that were made by the typesetter (e.g., transposition of letters, misspellings, misreading of manuscript). This should be done by writing P.E. and circling it. This will prevent printing errors from being charged to author alterations.
3. Fax or mail your final corrections to the address below: within 5 days of your receipt:

**NICK BARBER  
TECHSET COMPOSITION LTD.  
CHALKE HOUSE, 3 BRUNEL ROAD  
CHURCHFILEDS, SALISBURY, WILTS, UNITED KINGDOM  
FAX:011-44-1722-323159  
PHONE: 011-44-1722 332949**

**FAX OR RETURN WITHIN 5 DAYS OF RECEIPT BY EXPRESS MAIL.**

If you have questions about the enclosed materials or the book, contact Lisa Van Horn at  
Tel: (908) 813-1099; Fax: 908-813-1099 and email: [lvanhorn@wiley.com](mailto:lvanhorn@wiley.com) or  
Professor Akay at [metin.akay@asu.edu](mailto:metin.akay@asu.edu)

**Your cooperation in meeting the schedule requirements is very much appreciated.**



# *HYBRID OLFACTORY BIOSENSOR USING MULTICHANNEL ELECTROANTENNOGRAM: DESIGN AND APPLICATION*

*John R. Hetling, Andrew J. Myrick, and Thomas C. Baker*

## **15.1 INCORPORATING NEURAL CELLS AND TISSUE IN HYBRID DEVICE DESIGNS**

The term *biosensor* is used to describe a sensing system comprised in part of living matter or of materials derived from living matter (e.g., enzymes, antibodies, nucleic acids). Generally, the actual sensing element (i.e., front end) in the system is living, and the response of the living component is transduced by a second conventional sensor (e.g., an electrode) and the signal is measured and stored electronically [1]. Living organisms can be quite robust in terms of their ability to maintain homeostasis in a wide range of environments, but isolated cells, tissues, and organs require special consideration to keep alive when isolated from the parent organism. However, it is primarily single cells that are targeted for inclusion in biosensors. A reasonable conclusion is that biosensors are bulky given the significant amount of instrumentation required to keep isolated cells alive and quite fragile under field conditions where a sensor might be used. So what motivates the development of biosensors? The answer includes high sensitivity, high specificity, and speed. The same exquisite sensitivity to individual species of molecules in the surrounding milieu which allows a cell to play its particular role in the physiology of an organism can be exploited to detect those molecules in the parts-per-billion range, and this can often be accomplished on a millisecond time scale.

All cells are sensitive to environmental parameters such as pH, temperature, and toxins (any element or compound becomes a toxin at sufficiently high concentration) as well as basic metabolic compounds (e.g., glucose, oxygen, carbon dioxide). However, many cells are specifically sensitive to certain chemicals for which they express membrane-bound receptors (e.g., glutamate receptors expressed by cortical neurons) or certain types of energy (e.g., light sensitivity of retinal photoreceptor cells, stretch sensitivity of muscle spindle cells). A principal design feature of a sensor is its specificity, or the degree to which its output can be influenced by inputs other than the desired measurand. In other words, if you are building a biosensor to measure glucose, you would not want the sensor to also be sensitive to oxygen concentration unless you could absolutely control for

oxygen concentration in your system. The specificity of membrane-bound receptor proteins is another advantage of cell-based biosensors.

The choice to use a biosensor depends on whether the sensitivity, specificity, and speed offset the fragility, bulky nature, and expense inherent to their use. A primary motivation in biosensor research is to improve durability and reduce size and cost. The specific type of biosensor to be described here is designed to measure airborne chemicals, or odors. The approach is slightly different from most biosensor development in that the living component is the entire olfactory organ of an insect, the antenna. The biological response to an odor is a change in membrane potential of olfactory neurons contained within the antenna, and this biopotential can be recorded with electrodes. The system for recording the electroantennogram (EAG) as well as an EAG analysis approach allowing discrimination between different analytes (airborne volatile compounds) will be described in detail below.

## 15.2 APPLICATIONS FOR OLFACTORY SENSORS

---

Olfaction is the sensing of airborne molecules; an olfactory sensor is distinguished from a taste sensor in that it does not need to contact the solid or liquid source of the detected molecule. As many compounds of interest exhibit some degree of volatility, an olfactory biosensor can be thought of as a remote sensor. Potential applications of olfactory biosensors include and surpass applications of artificial sensors, assuming their inherent disadvantages can be overcome (there are theoretical and technical limitations on the size, sensitivity, specificity, and speed of artificial sensors). Industrial uses include quality control of aromatic products (e.g., perfume, wine) and environmental safety (a more refined approach to the canary in the coal mine). Airports routinely use an artificial olfactory biosensor in screening luggage for explosives and drugs (your bag is swabbed with a small white pad, which is then scanned for the illicit substance). Olfactory biosensors are sensitive to a long list of anthropogenic compounds of interest to security and defense, including drugs, explosives, and chemical warfare agents. For many insects, the ability to locate specific species of plants, or even individual plants in a certain state of health or maturity, is important for food or in their reproductive cycle; this is often accomplished by sensing airborne volatiles. Similarly, the body gives off specific odors depending on the state of health (e.g., ketones on the breath of diabetics). Olfactory biosensors may find use in the clinic either for rapid screening or as a high-level diagnostic tool.

## 15.3 STRATEGIES FOR ARTIFICIAL NOSE DESIGN

---

The artificial nose, as presently conceived, can be distinguished from other chemical detectors (such as pH or NO electrodes) by the promise of detecting an arbitrary number of different compounds with the same device. Where single-chemical detectors often rely on a semipermeable membrane specific to the molecule to be detected, artificial noses generally consist of an array of semiselective, cross-reactive sensors which demonstrate distributed specificity. There are a number of different artificial nose technologies currently being developed (see Table 15.1) [2–5]. An array of different classes of sensors yields a set of response vectors representing the sensor output, which must then be interpreted by a pattern recognition scheme. This has been done by using pattern recognition methods based on statistical and computational neural network approaches [5]. Current trends in artificial nose development include the use of temporal features in the

**TABLE 15.1 Signal Transduction Technologies in Use or Under Development for an Artificial Nose [5]. Each Approach Incorporates Multiple Sensor Classes with Differing Sensitivity Spectra Based on Variations in the Sensor Component which Interacts Directly with the Analyte (i.e., Odor). For Example, Attachment of Various Functional Groups to the Backbone of Conducting Polymers to Create Unique Polymers with Differing Affinity for a Given Analyte. Each Class of Sensor Within a Given Approach Requires Individual Fabrication; Individual Sensors Then Need to be Combined into One Device. This Labor-Intensive Process Imposes a Practical Limit of About Three Sensor Classes within a Given Device. This in Turn Limits Discrimination Across Broad Categories of Analytes**

Signal transduction technology	Principal of operation	Primary limitations
Metal-oxide and MOSFET	Electrical resistance of semiconductor changes when analyte molecules are adsorbed onto surface	High power levels required damaged by sulfur-containing compounds and weak acids Low sensitivity
Conducting polymers	Electrical conductance of film changes with reversible adsorption of analyte molecules	Long response times Drift Poor reproducibility Expensive
Piezoelectric-based (acoustic wave devices)	Analyte molecules adsorbed by thin films on crystals, altering RF resonance frequency	Drift Low sensitivity Poor reproducibility
Fiber-optic/solvatochromic fluorescent dye	Analyte molecules alter polarity of dye's surroundings, affecting fluorescence	Low sensitivity Long response times Limited lifetime (photobleaching)

detector response and the development of neural networks which can learn new odors on-line, without the need to retrain the entire odor library [5].

However, as noted in Table 15.1, there are three important limitations of artificial nose technology. First, the long response times (tens of seconds to minutes) of most approaches limit them to steady-state measurements, where the steady state may take impractically long times to reach. Steady state is not often attained under many field conditions where an artificial nose might find application (e.g., a turbulent wind stream). Second, the number of sensor classes comprising the array is limited to about three in present designs. This limits the number of compounds which can be distinguished and generally requires advanced knowledge of the compounds to be detected. Third, all artificial nose technologies exhibit low sensitivity as compared to most biological olfactory sensors.

## 15.4 BIOLOGY OF INSECT OLFACTORY SYSTEM

As stated above, the olfactory biosensor described here uses an insect olfactory organ, or antenna, as the sensing element. A brief description of the anatomy and physiology of this system will be helpful. The principal arrangement of the biological olfactory system is quite well conserved across phyla, from insects to mammals. Olfactory receptor neurons (ORNs) exhibit a response when airborne molecules bind to metabotropic membrane receptors and activate G-protein cascades, providing amplification and eventually leading to membrane potential changes and characteristic trains of action potentials

[6–8]. The antenna is comprised of a cuticle layer, contiguous with the rest of the insect exoskeleton, which contains the dendrites of the ORNs. Contact with the environment is made through a large number of fenestrations or pores in the cuticle; airborne compounds diffuse through the pores and to the dendrites. If the receptor protein expressed by an individual ORN binds to the odorant molecule, a G-protein-mediated transduction cascade, very similar to the phototransduction cascade in photoreceptor cells, results. A single activated G-protein acts on many (hundreds to thousands) substrate molecules, thereby providing a level of molecular amplification to the odor signal; this amplification is one reason a biosensor is inherently very sensitive. If the stimulus is strong enough, that is, enough receptor proteins were bound, threshold is reached and an action potential results.

These sensory neurons synapse onto a variety of interneurons in the antennal lobe (AL), the output of which appears on mitral cells which lead to higher processing structures in the brain. Sensory cells, numbering in the hundreds of thousands, have overlapping, semiselective, yet broad response spectra. The result of the transduction-level coding and the olfactory bulb processing is a system that exhibits a remarkably high sensitivity with broadband detection and discrimination. These are desirable features in any detector system and represent active areas of research in many areas of information technology.

## 15.5 BIOLOGICAL OLFACTORY SIGNAL PROCESSING

---

The ORNs, numbering around a few hundred thousand, may be divided into a smaller number of groups defined by the receptor protein expressed by each cell. There are about a hundred individual receptor proteins for the average insect. Each ORN expressing a given receptor protein projects axons to a specific glomerulus in the AL. These glomeruli are the first synaptic relay in the insect olfactory system and are analogous to the olfactory bulb in mammals. Each glomerulus is therefore “tuned” to the sensitivity spectrum of a particular receptor protein. Projection neurons carry the olfactory information from the AL to the mushroom body, where, through a set of feedback mechanisms, the representation of the odor in the neural coding space is refined before being passed on to higher perceptual levels.

This refinement of the neural representation of an odor, well described in a review by Laurent [9], is necessary because organisms are in general capable of discriminating between a number of odors that greatly exceeds the number of different receptor proteins. That is, each odor does not have a “hard-wired” connection to a perceptual center. This is possible because each receptor protein does not bind to only one specific molecule but has a finite sensitivity spectrum. A single receptor protein can bind to a family of compounds which differ slightly in molecular shape and charge distribution; these differences define the parameter space of odorant molecules. The parameter space of odors (i.e., the molecular properties of odorants to which sensory neurons are sensitive) is not precisely defined. However, structure–activity studies (chain elongation, double-bond position, functionality) performed on noctuid olfactory neurons *in vivo* have been particularly enlightening in understanding that ligand–receptor interactions can behave according to conformational energy and electron distribution models and not merely to space filling [10–12]. In short, some compounds bind more strongly than others, and a plot of binding efficiency versus variation in specific molecular parameters results in the sensitivity spectrum of a given receptor

protein. By interpreting the relative responses of several ORNs, each expressing different receptor proteins, a specific odor can be identified as unique.

## 15.6 PROOF OF CONCEPT FOR MULTICHANNEL EAG: DIFFERENTIAL SENSITIVITY BETWEEN SPECIES

---

The potential utility of using insect antennae as sensitive and *discriminating* biosensors for known agents in the environment stems from the successful use of the single-antenna EAGs that have been used to monitor the relative concentrations and even plume structures of high concentrations of known pheromone odorants (to which the selected EAG detector was tuned) [13–16]. An EAG response is thought to result from the summed generator (DC) potentials of individual olfactory receptor neurons that have been depolarized by exposure to an odorant, with the depolarizations of those receptor neurons closest to the recording electrode contributing more to the amplitude than those further away [17]. It has long been known, however, that EAG responses to any series of compounds form a graded series and are not compound specific. Even for sex pheromone components, the most specific of behaviorally active odors for insects, anthropogenic analogs differing significantly by chain length or functional group have been shown to be capable of generating significant EAG responses having amplitudes that are only 50–25% reduced from the natural pheromone compound itself [18].

Previous studies have hinted that EAG response spectra to a range of odorants can be at least a little species specific [19–21]. However, the concept of creating a discriminating EAG biosensor system by using an array of antennae that compares response amplitudes across the array had only very recently been suggested and attempted [22]. A discriminating EAG formed by antennae from multiple species would require exploiting only very slight species-to-species differences in the EAG response. Obviously, a single EAG signal from a very broadly tuned antenna responding in graded fashion to a wide variety of odorants cannot be used to discriminate one volatile compound from another.

Park et al. [22] created a discriminating EAG biosensor by utilizing differences in the EAG responses of several antennae from different species of insects monitored simultaneously. Their system made optimal use of the ability of the EAG to respond to sharp peaks in concentration such as those generated by the flux from individual odor strands in an odor plume passing over the antennae [13]; two or three depolarizations (i.e., odor strands) per second were registered. As shown by Baker and Haynes [13], the ability of an insect antenna to respond quickly to peak concentration in the strands in a plume makes it a much more sensitive system than slower responding artificial sensors whose polymers can only take a reading of time-averaged mean concentrations [23, 24].

The proof of the insect antennal array concept came when Park et al. [22] were able to discriminate most of the 20 different compounds they tested by comparing EAG response spectra across only five different species. The 20 compounds were presented as single puffs to individual antennae (Fig. 15.1), and the mean amplitudes of response to each compound over several replicates were calculated and normalized with respect to EAGs from a standard compound. The histograms developed from this process resulted in clear patterns of relative EAG amplitudes across the five species' antennae used. Most of these were discriminable by eye (Fig. 15.2).

Park et al. [22] then used simple clustering algorithms on the EAG amplitude information alone and confirmed what was apparent by eye. The cluster analysis

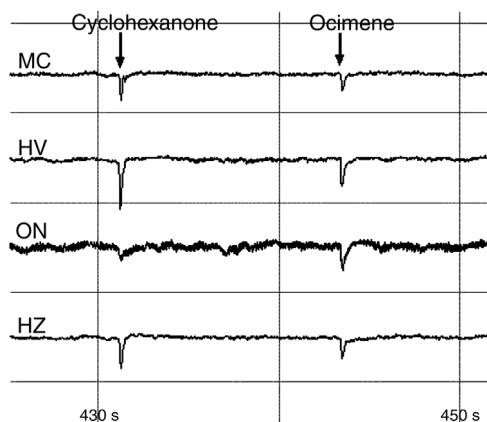


Figure 15.1 Differential EAG response amplitudes when either cyclohexanone or ocimene was puffed over antennae of *Microplitis croceipes* (MC; parasitic wasp), *Heliothis virescens* (HV; moth), *Ostrinia nubilalis* (ON; moth), or *Helicoverpa zea* (HZ; moth). Each horizontal division is 5 mV, and each vertical division is 10 s.

clearly demonstrated that compounds from similar classes (such as medium-chain-length aliphatic alcohols and longer chain length aliphatic alcohols) clustered together (Fig. 15.3). They also showed that compounds within classes were distinguishable based on characteristics such as chain length (Fig. 15.3).

Thus the proof of concept for using a multichannel EAG to discriminate between an arbitrary number of odors had been established. However, several technological issues needed to be addressed to make the EAG biosensor practical. Principal among these were the design of a multichannel electrode array and preamplifier optimized for field condition recording of the EAG and the automation of the odor discrimination analysis. Electronic optimization of the preamplifier will assure that the extreme sensitivity of the antenna can be exploited [i.e., maximize the signal-to-noise (SNR)]. Colocalization of antennae will assure that an odor strand in a turbulent air stream is sensed by each antenna at approximately the same time. Minimizing the size of the preamplifier will minimize perturbations to the air stream. Automation is important in order to take advantage of the inherent speed of the hybrid system and to fulfill many potential applications requiring

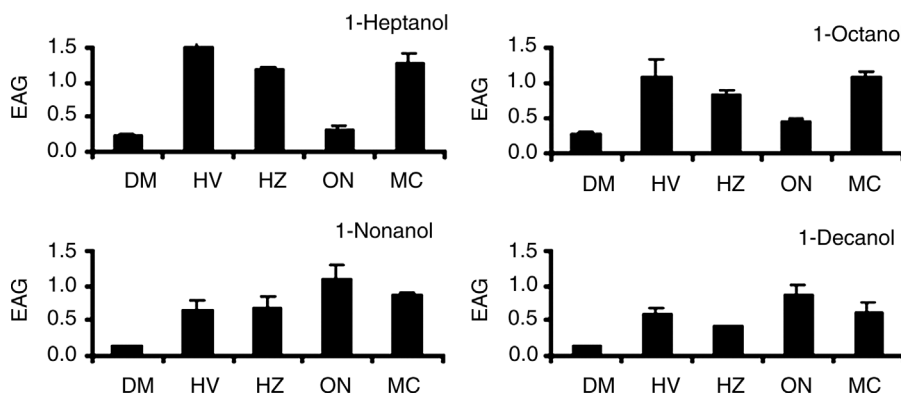


Figure 15.2 EAG response amplitudes from five different insect species' male antennae when presented with four different straight-chain alcohols: DM = *Drosophila melanogaster*, HV = *Heliothis virescens* (moth), HZ = *Helicoverpa zea* (moth), ON = *Ostrinia nubilalis* (moth), and MC = *Microplitis croceipes* (parasitic wasp).

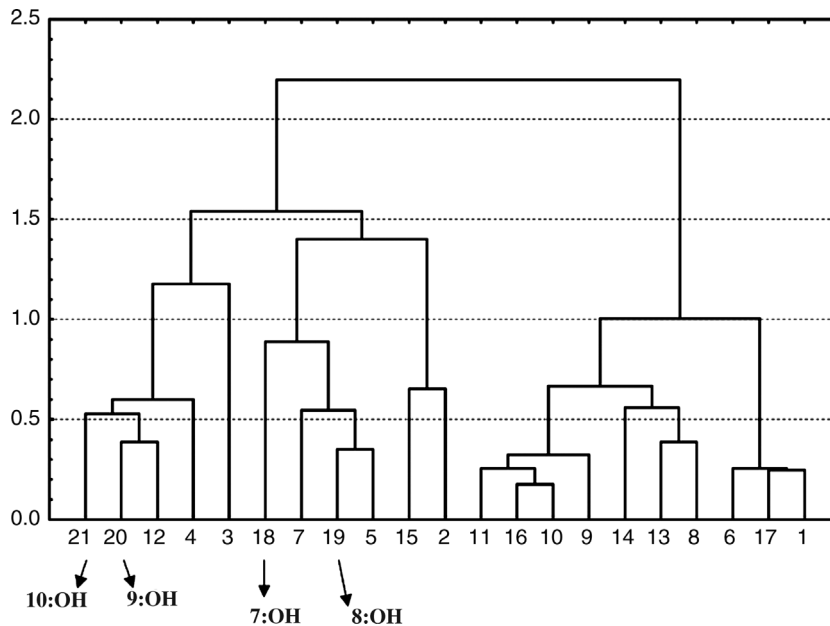


Figure 15.3 Cluster analysis of five-species EAG response profiles to 20 different volatile compounds. Decanol (10:OH) and nonanol (9:OH) cluster together but separate from octanol (8:OH) and heptanol (7:OH). Visually this should be apparent in Figure 15.2. Compounds 8–11 and 13 are all monoterpenes, sitting in a separate cluster of EAG antennal array response patterns than the aliphatic alcohols.

autonomous operation (e.g., roving robots searching for land mines). Early answers to each of these challenges are described in the following sections.

## 15.7 DESIGN OF MULTICHANNEL EAG SYSTEM

In the design of an EAG acquisition system, it is desirable to maximize the SNR obtained. It is also desirable to eliminate or limit as many sources of interference as possible. Minimization of noise and interference allows maximal information to be extracted from the signal during postacquisition processing. The source of noise is in the physical components that take part in processing the input signal, while interference originates outside the signal path. Sources of interference include 60-Hz power-line radiation, radio-frequency radiation, electronic changes due to temperature drift, mechanical agitation, and power supply ripple. Noise sources are numerous but often include thermal (Johnson) noise,  $1/f$  or flicker noise, shot noise, and quantization noise.

A further source of interference arises from inside the “sensor” (i.e., the antenna), which contains not only chemoreceptors but also mechanical receptors. As air is swept across the antenna, mechanoreceptors are stimulated, giving rise to a source of interference in this application that cannot be eliminated. A source of signal noise is likely to be related to the origin of the signal. The EAG voltage changes are caused by ensembles of individual action potentials. The number of neurons involved appears to be on the order of  $10^5$ , probably an order of magnitude less for any individual response (referred to below, by convention, as a *depolarization*). Together, the number of neurons and their firing rate

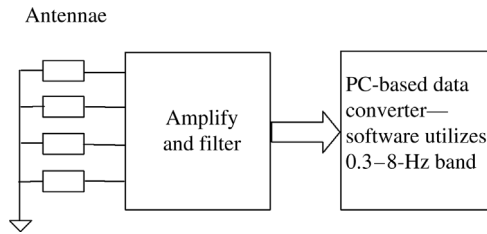


Figure 15.4 EAG acquisition system block diagram.

present a fundamental limit to the amount of information that can be obtained from the signal. Despite the inherent sources of distortion in the sensor, it is still desirable for research purposes to provide the most accurate EAG measurements possible by limiting electrical sources of interference and noise.

Biopotential amplifiers are traditionally located remotely from the signal source, which is connected via shielded cables to a differential amplifier. A long cable has a tendency to pick up interference, or generate interference as a result of mechanical agitation, known as the triboelectric effect. Further, a differential amplifier (two amplifiers per channel) is needed to reduce power line interference. In the EAG application, a single ended active probe can amplify the signal very close to its source, which is also physically small, and send a much higher power signal through a cable for further amplification and filtering. The power gain is high enough to overpower interference sources. For instance, the power gain of the EAG active probe described here, with  $500\text{ k}\Omega$  input resistance, is  $2 \times 10^7$ . Another advantage to this approach is that only one preamplifier per channel is needed. Further, amplifier bias current is provided through the antenna itself without the need for biasing circuitry.

Q2

A good way to begin a design is to first draw a general block diagram (Fig. 15.4). The hardware component to be described here is the “amplify-and-filter” section. The PC-based converter is readily available from many vendors. The amplifier interfaces with the antennae at its inputs and the data converter at its outputs. To begin designing, it is first necessary to characterize both the antennae and the data converter.

Figure 15.5 shows a Thevenin equivalent circuit for a typical insect antenna. The antenna acts as a voltage source,  $V_A$ , in series with a source resistance,  $R_A$ . The Thevenin equivalent resistance can be expected to vary from approximately  $100$  to  $10\text{ M}\Omega$ . This value also varies as the preparation becomes less viable through dehydration and so cannot be easily predicted. Noise that is present across any source of real, finite impedance is termed Johnson noise, which is created by thermal motion of charge carriers. This noise cannot be avoided without reducing the temperature of the source. Johnson noise has equal power density at all frequencies (up to the terahertz range) equal to  $4kT$  watts per hertz.

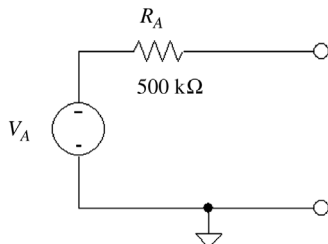


Figure 15.5 Thevenin equivalent circuit for insect antenna.

The root-mean-square (RMS) value of the Johnson noise voltage spectral density across any resistor can be calculated using

$$V_J(f) = \sqrt{4kTR} \quad \text{V}/\sqrt{\text{Hz}}$$

where  $k = 1.38 \times 10^{-23}$  is Boltzmann's constant and  $T$  is temperature in kelvin. For example, the noise level of the resistor value  $R_A = 500 \text{ k}\Omega$  from 0.1 to 10 Hz at 298 K is

$$V_J = \sqrt{(4)(1.38 \times 10^{-23})(298)(500 \times 10^3)(10 - 0.1)} = 285 \text{ nV RMS}$$

The voltage  $V_A$  may also be further characterized. The EAG signal has an approximate "active" level of 400  $\mu\text{V}$  RMS and occupies the frequency range of about 0.1–10 Hz. The maximum signal swing expected is approximately 10 mV peak to peak (p-p). In addition, a large DC offset on the order of 100 mV is typically present on the EAG signal.

A useful comparison between the signal and the noise is the SNR, often expressed in decibels:

$$\text{SNR} = 10 \log_{10} \left( \frac{S}{N} \right) = 20 \log_{10} \left( \frac{V_S}{V_N} \right)$$

where  $S$  represents the signal power,  $N$  represents the noise power, and  $V_S$  and  $V_N$  are the signal and noise voltages, respectively. Here, for example,

$$\text{SNR} = 20 \log_{10} \left( \frac{400 \times 10^{-6}}{285 \times 10^{-9}} \right) = 63 \text{ dB}$$

Now the input characteristics of the data converter can be summarized. A simplified analysis can be divided into two parts: the amplifier and the digitizer. Although it is difficult to know the exact analog signal input chain to the analog-to-digital converter (ADC) within a proprietary digitizer design, a good model may be constructed by treating each analog channel as an independent amplifier followed by a first-order low-pass filter (LPF), with negligible noise above the corner frequency of the LPF. Because the floating-point digital output of the digitizer software driver is scaled to the input voltage, the gain of the amplifier is unknown and does not need to be determined. If necessary, it would be possible to determine the gain by measuring the quantization levels and opening the digitizer case to find the ADC part number to determine its input range.

The greatest concern in designing the amplifier is the noise it adds to the input signal. Generally, the input noise voltage  $V_N$  and sometimes the input noise current  $I_N$  of an amplifier are specified as functions of frequency. Often  $V_N$  consists of so-called *flicker noise* and *white-noise* components. For input source impedances that are very high  $I_N$  is a concern. In this case, it is expected that the input of the digitizer amplifier will be driven by a low-impedance amplifier output from the "amplify-and-filter" stage. Flicker noise density can be approximated with the equation.

$$V_{Nf}(f) \cong K \sqrt{\frac{1}{f}}$$

White noise, by definition, has a flat spectral density, as in the relation

$$V_{NW}(f) \cong N_W$$

The RMS values of two independent noise sources in series can be represented as a single noise source with an RMS value equal to the sum of their squares. Therefore, the total

equivalent input noise density is given by the formula

$$V_N(f) = \sqrt{K^2 \frac{1}{f} + N_W^2}$$

Further, the bandwidth of any real amplifier is limited. A simple way to model this bandwidth limitation is to place a first-order LPF on the output of the amplifier (gain 1). The “output” noise spectral density curve shown in Figure 15.6 is an estimate of the amplifier noise present at the scaled output of the digitizer with the amplifier input grounded. Such a curve is plotted in the figure. Parameters of the input amplifier and multiplexer chain are as follows:

Input referred white-noise spectral density	250 nV/ $\sqrt{\text{Hz}}$
Input referred flicker noise coefficient	$3.75 \times 10^{-6}$ W
Amplifier bandwidth	413 kHz
Input impedance	100 G $\Omega$ /100 pF
Bipolar input voltage ranges	$\pm 50$ mV, $\pm 0.5$ V, $\pm 5$ V, $\pm 10$ V

Parameters of the digitizer are as follows:

Analog input channels	16
Maximum sample rate (total for all channels)	200,000 samples/s
Sampling resolution	16 bits
Accuracy	$\pm 3$ LSBs (least significant bits)

Typically, the signal power and the noise power are compared within a specified bandwidth, where the signal power exists. A noise voltage spectral density may be integrated across a frequency range using the equation

$$V_{NBW} = \sqrt{\int_{BW} V_N^2(f) df}$$

Fortunately, in this application, quantization noise is not a problem. At a sample rate of 12,500 samples/s, 67 aliased segments of the amplifier white noise integrate from 0.1

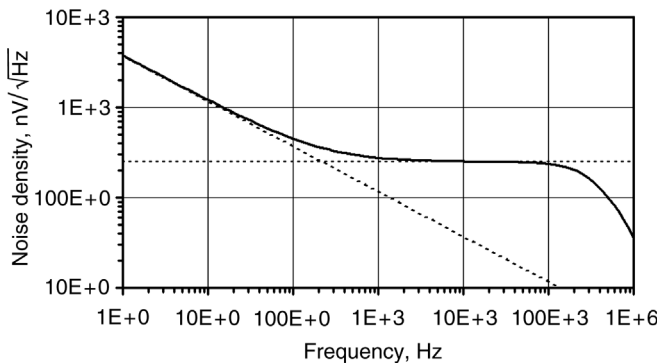


Figure 15.6 Spectral density estimate of digitizer output noise.

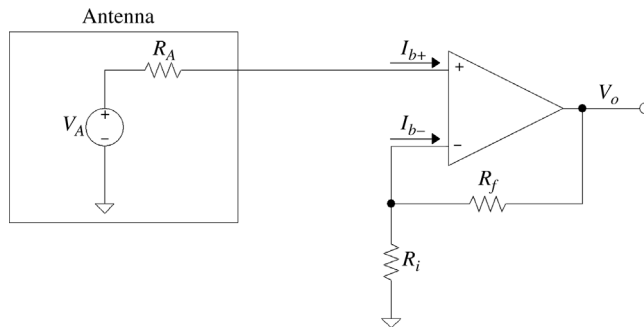


Figure 15.7 Preampifier connected to antenna equivalent circuit.

to 10 Hz, resulting in 6.4  $\mu\text{V}$  RMS. The  $1/f$  noise integrates to 8.0  $\mu\text{V}$  RMS. The total noise is

$$V_N = \sqrt{(6.4 \times 10^{-6})^2 + (8.0 \times 10^{-6})^2} = 10.2 \mu\text{V RMS}$$

Without precise knowledge of the source impedance of the antenna, an amplifier with very high input impedance is desirable to measure the EAG voltage accurately. Illustrated in Figure 15.7 is a model of an antenna connected to a noninverting high-input-impedance amplifier. The performance of this amplifier construct is highly dependent on the performance of the operational amplifier (op amp). The performance of an op amp can be evaluated by examining parameters assigned to its nonideal behavior.

Every op amp requires bias current to operate its input amplifiers. This is usually specified on manufacturer’s specifications as “input bias current.” Further, each individual amplifier has an impedance to ground and an impedance between itself and other amplifier inputs on the same device. These are known as “common-mode input impedance,” and “differential-mode input impedance,” respectively. The degree of power supply ripple and noise feedthrough to the op amp output is usually specified as the power supply rejection ratio (PSRR). Other parameters critical to this application include “input current noise” and “input voltage noise.” These will be explained in further detail below.

Before selecting an amplifier, it is a good idea to list the few critical specifications, which will aid in generating a list of candidate devices. Specifications of major concern are listed below. A point should be made that datasheet noise data are representative of a typical amplifier and are only approximate. Thus, consideration should be made for variability between individual parts.

Parts per pkg	4 in this application
Input bias current	$\leq 1 \text{ nA}$
$R_{CM}$	$\geq 1 \text{ G}\Omega$
In-band current noise	$\leq 40 \text{ fA RMS}$
Voltage noise	Evaluate
PSRR	Maximize

**Q3**

Noise sources in the noninverting amplifier configuration (excluding thermal noise in the antenna) (Fig. 15.7) include the resistors and the amplifier. Amplifier noise is measured and usually published in the op amp specifications. Measured amplifier noise includes input referred noise voltage and input referred noise current. In this application, the

noise at the amplifier output can be approximated using the equation

$$V_o \cong \left(1 + \frac{R_f}{R_i}\right) V_{NBW}$$

This equation applies only because the component values and amplifier specifications have been chosen properly. For more details on op amp noise analysis see Clayton [25] and the application note by Bob Clark [26] listed in the references.

Two particular op amps considered for this design were the AD8608 and the LMC6084. Integration of the noise from 0.1 to 10 Hz results in the following noise specifications (data shown for the LF147, used in a circuit second stage, will become relevant below):

Op amp	PSRR, dB	$I_N$ , fA/ $\sqrt{\text{Hz}}$	$K$ , nW	$V_{NBW}$ , nV RMS
AD8608	77	10	91.7	197
LMC6084	72	0.2	285	611
LF147		10	164	353

The SNR at the output of each amplifier has been calculated for an “active” signal input of 400  $\mu\text{V}$  RMS in the preamplifier for  $R_i = 10 \text{ k}\Omega$  and  $R_f = 100 \text{ k}\Omega$  and plotted in Figure 15.8 as a function of the input resistance. The SNR is a decreasing function of the input resistance because the available signal power is inversely proportional to the input resistance but the noise power is constant.

Q4

A figure of merit for an amplifier is its *noise figure*. The noise figure is expressed in decibels as

$$\text{NF} = 10 \log_{10} \left( \frac{S_i/N_i}{S_o/N_o} \right)$$

where  $S_i/N_i$  is the signal-to-thermal-noise ratio at the input of the amplifier. The noise figure is a measure of how much noise the amplifier adds to the signal over the thermal noise present at the input. The lower the noise figure, the better the amplifier. A perfect amplifier has a noise figure of 0 dB. In this case, the NF can be calculated using the

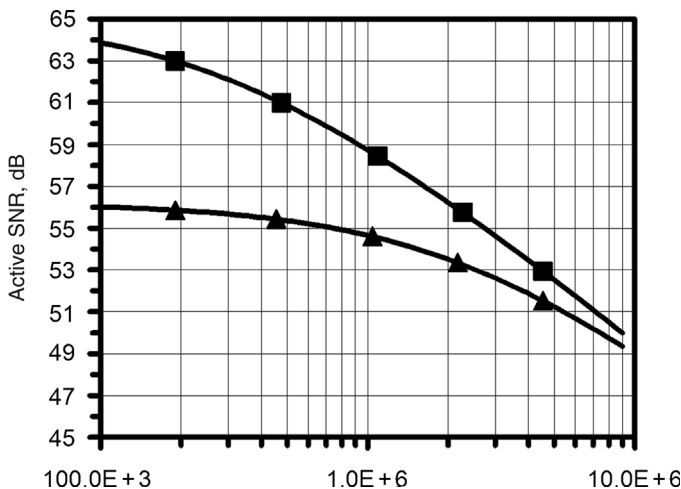


Figure 15.8 Preamplifier SNR as function of antenna resistance: ■, AD8608; ▲, LMC6084.

equation

$$NF \cong 10 \log_{10} \left( \frac{V_{NBW}^2}{4kTR_A BW} \right)$$

The noise figure of each amplifier considering input current noise and resistor network noise (i.e., not the equation above) as a function of the input resistance is plotted in Figure 15.9a. The noise figures for the AD8608 and LMC6084 are decreasing functions of the input resistance. There are two main contributors to noise for these two amplifiers:  $V_N$  and the Johnson noise of the antenna. As the resistance of the antenna increases, so does the Johnson noise voltage, which eventually dominates the noise at the output of the op amp. This means that the op amp does not add much significant power to the noise signal, resulting in a near 0-dB noise figure at 10 M $\Omega$ . Conversely, at  $R_A = 100$  k $\Omega$ , the Johnson noise voltage of the antenna is reduced by a factor of 10, and the amplifier input voltage noise dominates.

It is now appropriate to determine the necessary amount of preamplifier gain. Following the law of superposition, the system noise figure can be calculated by summing the noise sources at the output of the acquisition system and comparing it to the component at the output due to thermal noise at the antenna. The system output noise voltage  $V_{NS}$  can be calculated using the equation

$$V_{NS} = \sqrt{(V_{e0}A_2A_1)^2 + (V_{e1}A_2)^2 + V_{e2}^2} = \sqrt{A_1^2A_2^24kTR_A BW + A_1^2A_2^2V_{NBW}^2 + V_{e2}^2}$$

where

$V_{e0}$  = antenna input thermal noise voltage

$V_{e1}$  = equivalent output noise of preamplifier

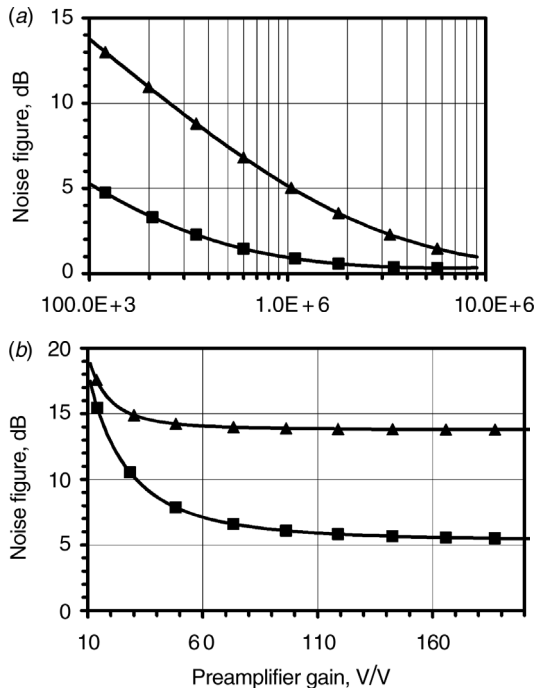


Figure 15.9 (a) Preamplifier noise figure as function of antenna resistance and (b) system noise figure as a function of pre-amp gain ( $R_A = 100$  k $\Omega$ ): ■, AD8608; ▲, LMC6084.

$V_{e2}$  = equivalent output noise of digitizer

$A_1$  = preamplifier gain

$A_2$  = digitizer gain = 1

We have already calculated  $V_{e2}$ , the equivalent output noise of the digitizer. This is 10.2  $\mu\text{V}$ . Since the output of the digitizer in the software is equal to the measured input, the gain of the digitizer,  $A_2$ , is 1. The system noise figure can be calculated using the formula

$$\text{NF} = 10 \log_{10} \left( \frac{V_{\text{NS}}^2}{A_1^2 A_2^2 4kTR_A \text{BW}} \right) = 10 \log_{10} \left[ 1 + 2.41 + \left( \frac{80.0}{A_1} \right)^2 \right]$$

where the worst-case antenna resistance value  $R_A = 100 \text{ k}\Omega$  has been selected. The first of the three terms is the thermal noise; the second is the added preamplifier noise, which has been minimized through selection of the amplifier; and the third contribution to the noise figure is the digitizer noise. To approach a perfect amplifier, effort must be made to minimize the second two terms. The second term is minimized by selecting the appropriate preamplifier part. The third term is minimized by selecting the gain. Intuitively,  $A_1$  needs to be increased until the noise due to the digitizer becomes insignificant compared to preamplifier and thermal noise.

When the gain is adjusted by varying  $R_i$ , the NF varies as in Figure 15.9*b*. It can be seen that the noise figure asymptotically approaches its minimum value as the gain is increased. But unfortunately, the DC voltage offset at the input can be expected to be up to 100 mV. The better device, the AD8608, can only operate at up to  $\pm 3 \text{ V}$ . So the maximum gain possible is approximately 20 V/V. Without the ability to use a high-pass filter (HPF) in this configuration with a reasonable capacitance value, the addition of a second amplification stage is needed. So the first-stage amplifier design is finalized with a gain of 21.

To squeeze out another 7 dB from the system, another gain stage is needed. But to eliminate the large DC offset, it is necessary to use a HPF. A 0.1-Hz first-order HPF will remove the DC offset and has a manageable settling time ( $\tau = 1.6 \text{ s}$ ) but distorts frequencies of interest in both magnitude and phase from 0.1 to  $\sim 1 \text{ Hz}$ . Even though component tolerances for a HPF are on the order of  $\pm 10\%$ , it is possible to remove most of the distortion in a software-implemented compensation filter [finite impulse response (FIR) described below]. The SNR measurements are subject to variation. Thus, a safe margin should be created in case the digitizer noise is higher or the preamplifier noise is lower than expected. Also, digitizer flicker noise is higher at lower frequencies, but the signal is attenuated more by the HPF. Using a gain of 11 V/V in the second stage results in an overall gain of 231 V/V and a maximum peak-to-peak signal range of 2.31 V, which is just outside the 2-V range of the digitizer. A HPF with a corner frequency of 0.1 Hz and a LPF of 20 Hz is used to help reject 60 Hz as well as an antialiasing filter that removes high-frequency preamplifier noise and other high-frequency interference that could alias into the 0.1–10-Hz band. To deal with all types of interference sources, it is desirable to attenuate as much as possible signal frequencies above  $f_s/2$ , where  $f_s$  is the sampling frequency. For instance, in our laboratory, a large ( $\sim 10\text{-mV}$ ) troublesome, wide-bandwidth 50-kHz interference signal is present that must be highly attenuated to avoid being aliased into the 0.1–10-Hz band when sampled at 12,500 samples/s. To preserve simplicity, we use a first-order filter (Fig. 15.10).

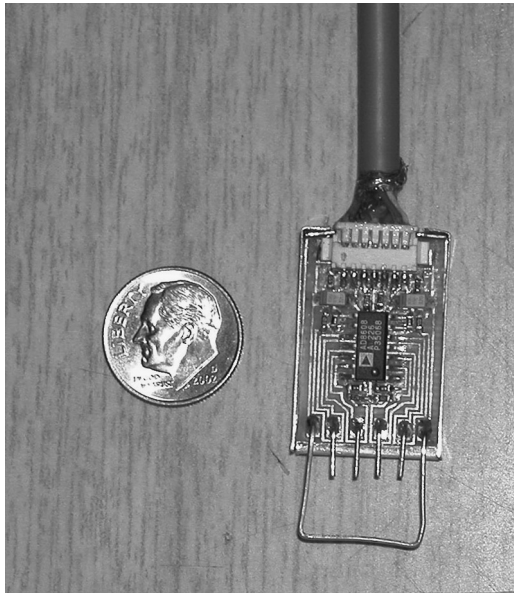


Figure 15.10 Second-stage amplifier schematic; first-order bandpass filter with gain.

The general-purpose junction field-effect transistor (JFET) quad op amp, the LF147, is used for the second stage. Using the worst-case antenna resistance  $R_A = 100 \text{ k}\Omega$ , the equations for the two-stage system output noise and noise figure are as follows:

$$V_{NS} = \sqrt{(V_{e0}A_3A_2A_1)^2 + (V_{e1}A_3A_2)^2 + (V_{e2}A_3)^2 + V_{e3}^2} = 55.3 \text{ }\mu\text{V}$$

$$\text{NF} = 10 \log_{10} \left[ 1 + \left( \frac{V_{e1}}{V_{e0}A_1} \right)^2 + \left( \frac{V_{e2}}{V_{e0}A_1A_2} \right)^2 + \left( \frac{V_{e3}}{V_{e0}A_3A_2A_1} \right)^2 \right]$$

$$= 10 \log_{10}(1 + 2.41 + 0.018 + 0.121) = 5.50 \text{ dB}$$

Variable	$V_{e0}$	$A_1$	$V_{e1}$	$A_2$	$V_{e2}$	$A_3$	$V_{e3}$
Equation	$\sqrt{4kTR_A BW_1}$		$A_1 V_{NBW1}$		$A_2 V_{NBW2}$		
Value	0.127 $\mu\text{V}$	21	4.14 $\mu\text{V}$	11	3.9 $\mu\text{V}$	1	10.2 $\mu\text{V}$

Q5

There are four terms involved in the above equations: antenna thermal noise, amplifier 1, amplifier 2, and the digitizer. It can be seen that most of the noise is due to the thermal noise and the stage 1 amplifier. For higher values of  $R_A$ , the noise performance of stage 1 will increase substantially.

Care is also taken to isolate the preamplifier from the power supply. Much of the power supply noise is removed by a voltage regulator and the PSRR of the amplifier. Fortunately, power supply ripple is  $\geq 60 \text{ Hz}$  and will be entirely removed by digital filtering after acquisition. The final EAG amplifier has the block diagram shown in Figure 15.11. The hardware design is complete; however, some signal processing is performed in the software. A block diagram of the signal chain connected to the EAG amplifier output is shown in Figure 15.12.

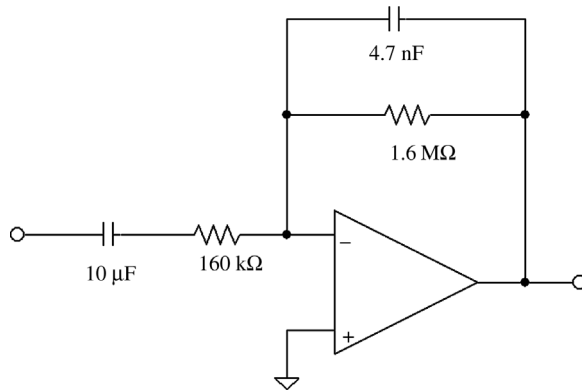


Figure 15.11 EAG amplifier block diagram:  $R_A$ , source impedance of antenna; HPF, high-pass filter; LPF, low-pass filter;  $f_c$ , cutoff frequency;  $G$ , gain.

Because we have more than adequate processing power in the average PC, a very sharp infinite-impulse-response (IIR) Butterworth LPF is employed (characteristics shown in Fig. 15.13). This filter will reduce any 60-Hz signal to well below the in-band amplifier noise level. After decimation, a FIR compensation filter removes distortion introduced by the 0.1-Hz HPF and the 20-Hz LPF in the second-stage amplifier. Nonuniform phase delay in the FIR filter is also compensated for. Compensation is applied from 0.1 to 30 Hz. It is after the compensation filter that the data are considered properly acquired and are recorded to disk for future review. The final design, after assembly on a printed circuit board, is shown in Figure 15.14. The circuit is contained in a slim aluminum case, and four antennae make electrical contact with the four amplifier input electrodes and the common ground electrode via conductive gel (as used with clinical electrocardiogram electrodes). The amplifier is connected via a seven-conductor cable ( $V^+$ ,  $V^-$ , ground, and four single-ended data channels) to the data acquisition card in a laptop computer for digital signal processing (Fig. 15.13) and execution of the algorithm which discriminates between odors based on the four-channel EAG data, as described in the following section.

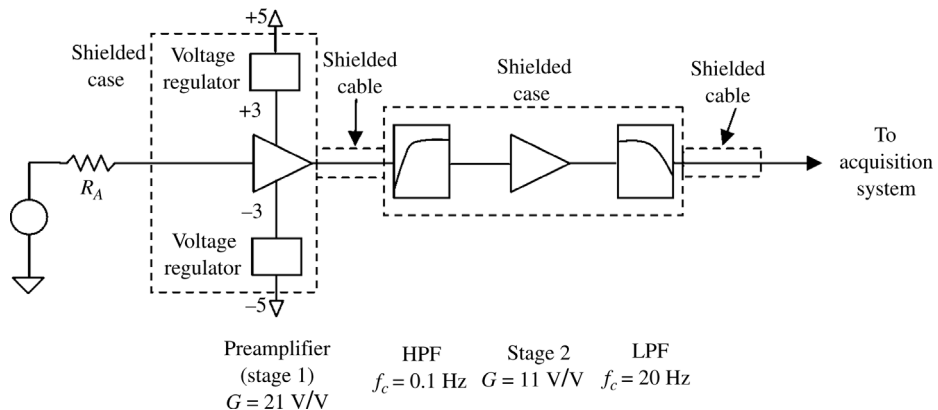


Figure 15.12 Data acquisition and processing system block diagram: FIR, finite-impulse-response filter.

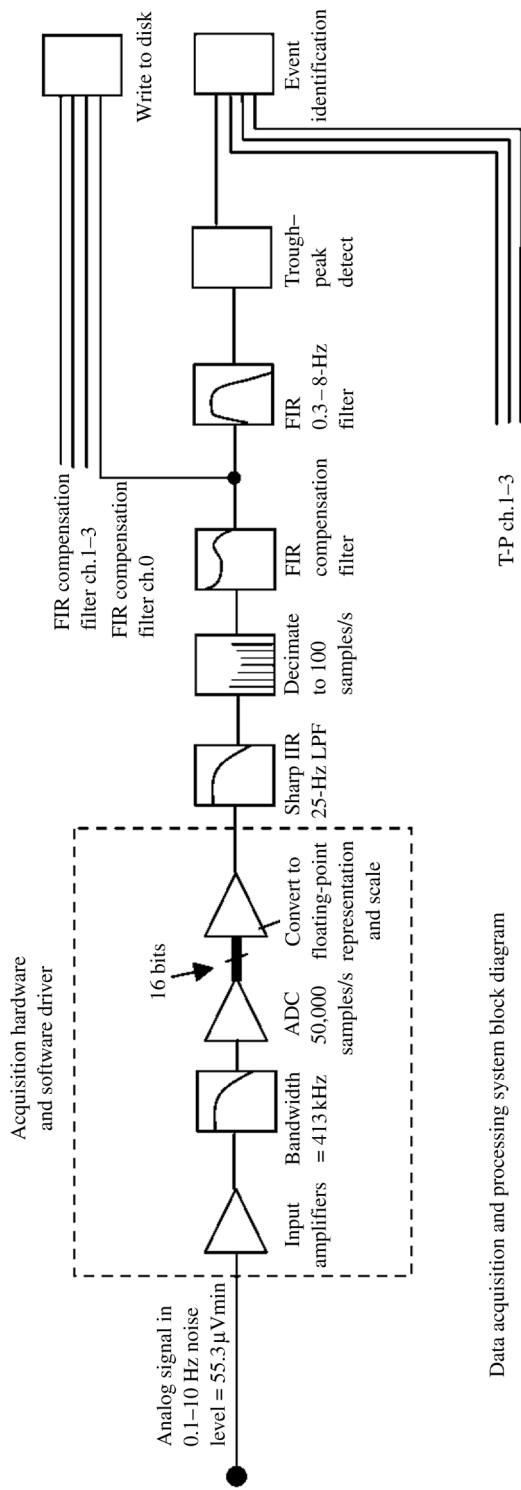


Figure 15.13 A 25-Hz Butterworth LPF, 20th-order frequency response.

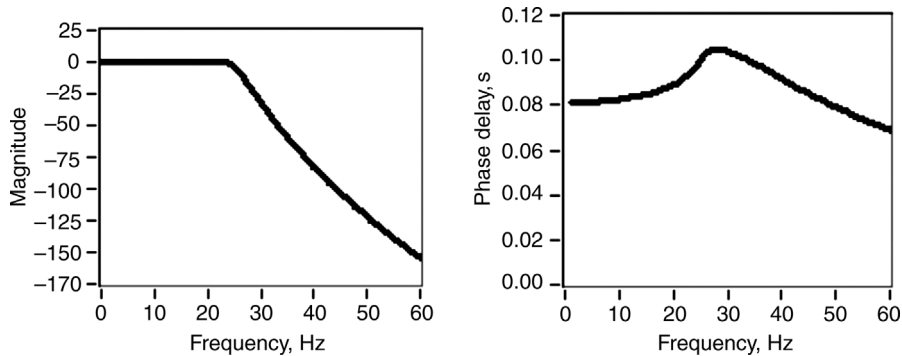


Figure 15.14 Final circuit design executed on custom printed circuit board using surface-mount components to minimize outside dimensions of entire package. The top of the case is removed; shown next to a U.S. dime for size comparison. When assembled, the case is less than 5 mm thick.

## 15.8 SIGNAL PROCESSING OF MULTICHANNEL EAG: AUTOMATED ODOR DISCRIMINATION

After the data are acquired, they are further processed to discriminate between odors. This is accomplished by identifying and measuring features of each response (depolarization) and then applying a relatively common pattern recognition technique. It should be noted that several strategies could be employed to discriminate odors based on EAG data, and the methods described below are only one solution. Other approaches are being investigated in our laboratory in an effort to maximize robustness, speed, and ease of implementation.

The objective of the signal processing level of the system is to identify EAG depolarizations, measure their amplitude, and group time-correlated depolarizations recorded from the four antennae. The time-correlated depolarizations correspond to a single odor strand passing the array of antennae. The correlated groupings of depolarizations are termed *events*. In order to associate the responses of the antennae with a particular odor, the system must first be trained. Training is accomplished by collecting data while subjecting the antennae to various known odor sources. After training has been completed, a classifier uses the training data to identify the odor that gave rise to the recorded event. The classification is performed on-line within 1 s after the data have been acquired.

The 0.3–8-Hz filter is noncausal and has approximately the frequency response depicted in Figure 15.15. The filter was constructed empirically and assists in peak-to-trough

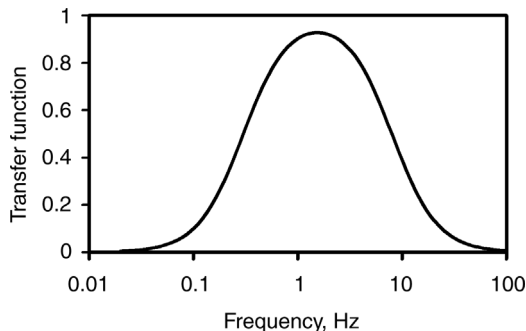


Figure 15.15 The 0.3–8-Hz bandpass filter frequency response.

detection by creating troughs that precede the peaks (purposeful distortion of the signal) and by smoothing the waveform. Most bandpass functions would accomplish these tasks.

A peak detection algorithm finds maxima and minima of polynomials fit to the data; the result is identification of the locations and values of the depolarizations. An example of this step is shown in Figure 15.16. The data are greatly reduced as only the peak-to-nearest-preceding-trough amplitude is retained, along with the time of the peak. These data are then compared to a threshold. Peak–trough events with an amplitude larger than a user-adjustable threshold are kept, while those smaller are considered to be unreliable and ignored.

Recall that events are comprised of the responses of the four antennae to a single strand of odor, which passes transiently across the array. Because the antennae cannot occupy the same point in space, the time of arrival of the odor strand and therefore the time of the four EAG response peaks are not coincident but depend on the air speed and the spacing of the antennae relative to the wind direction (and possibly, to a lesser degree, on species). Event identification is accomplished by associating peak–trough events that are close in time. The user may adjust this correlation time. The largest depolarization within a presumed event is then evaluated by another threshold to retain only events containing significant energy on at least one channel. Figure 15.17 depicts the result of evaluating the four EAG signals for “near-simultaneous” EAG responses which would comprise an event. Only the trough-to-peak amplitudes for the four channels are plotted (filled symbols), along with markers to denote the time of detected events (open circles). Note that in this example the event time window is 16 ms, and the event markers are plotted 16 ms following the last depolarization which is a component of each detected event. That is, depolarizations recorded more than 16 ms apart would not be considered to arise from the same odor strand. The choice of time window is influenced by wind speed and the distance between the most upwind and downwind antennae in the array.

Classification techniques utilize “features” and “classes,” where it is hoped to classify an event based on its features. In this application, the features used to describe the odor are the depolarization (peak-to-trough) amplitudes of the four preconditioned EAG signals. Thus, each event is described by four features. Each feature can be considered one dimension in a multidimensional feature space. Odors that can be discriminated have high probability density in different regions of the feature space. Bayes’s theorem can be used for classification if the probability distributions of each class are known. Ideally, during training, a four-dimensional histogram could be produced. Unfortunately,

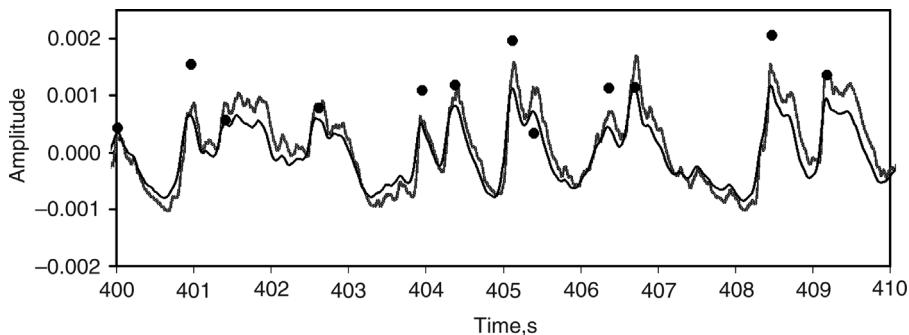


Figure 15.16 Segment from typical one-channel EAG recording. Light trace is the raw signal, dark trace is after filtering. Filled circles indicate times and trough-to-peak magnitudes of responses which were above the user-defined threshold (100  $\mu\text{V}$  in this case).

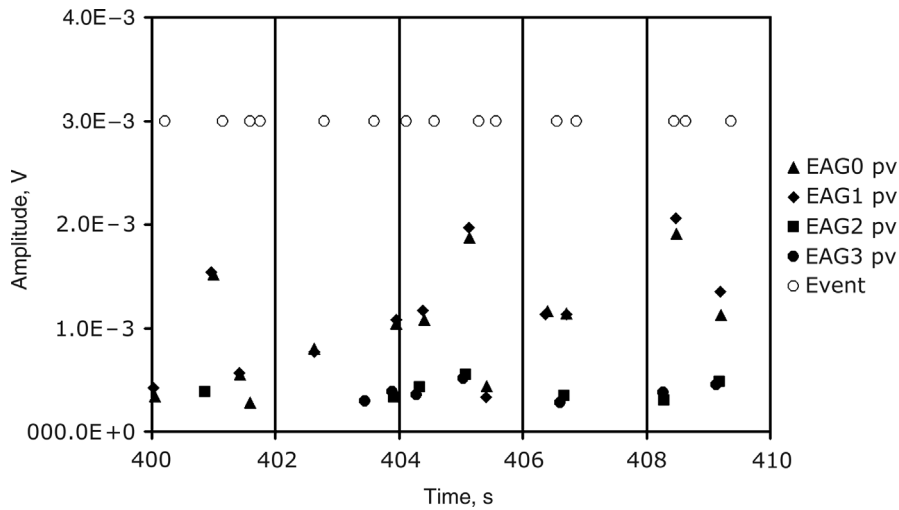


Figure 15.17 Trough-to-peak values (filled symbols) and event time markers (open circles) obtained with a 16-ms correlation time. Events markers are located 16 ms after the last trough-to-peak value contained in that event.

the number of data points required to create an accurate four-dimensional histogram (or up to 16 dimensions) is prohibitive. Thus, alternate classification techniques are available. One such technique, known as the “ $k$ -nearest-neighbor” technique, was employed here.

The measured features of each event are plotted in four-dimensional space, where each dimension represents one channel (i.e., antenna). The training data are collected first, which involves exposing the sensor to known odors, sequentially, until a requisite number of training events have been collected. In the example presented here, 100 training events were recorded for each odor, which took 1–2 min per odor; any number of odors can be contained in the training set.

The classification technique uses the weighting function  $X_{d1-d10} = 1/(d + 20 \mu\text{V})$ , where  $d$  is the “city block” distance of the point to be classified to training data points in the four-dimensional feature space. The city block distance between two points is the sum of the absolute value of the difference between every dimension. For instance, in just two dimensions,  $d = |x_2 - x_1| + |y_2 - y_1|$ , which is the distance you would have to travel in most places in Chicago to get from  $p_1$  to  $p_2$ . Ten values of  $X$  are calculated for each odor in the training data. These 10 values are summed for each training odor, and the unknown point is classified as being the training odor associated with the maximum sum. Presently, the classifier assumes equal prior probabilities, and the training data are not normalized. Also, the coefficient in the weighting function is chosen manually. Automating these aspects of the algorithm is a future goal.

The results of a simple classification experiment are shown in Figure 15.18. Here, the system was trained with three odors. The odor stream was created by placing a drop of one of three volatile liquids on each of three pieces of filter paper that were placed, in turn, about 5 ft upwind in an indoor wind tunnel, giving rise to odor A, odor B, and odor AB. Exhaust from the wind tunnel was vented to the outside, preventing an odor from recirculating in the air stream. Due to turbulent flow, at times the antennae are stimulated by the introduced odor strands, while at others, the array is detecting only components of the room air. As a result, the training data are not pure and represent mixtures of room air and the intended odorant. This presents a problem, because an

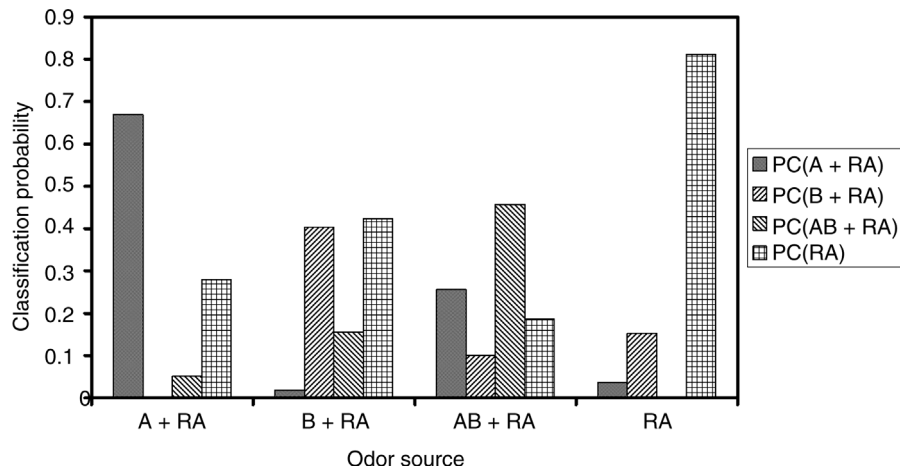


Figure 15.18 Classification results when system was trained on three odors (A, B, and AB) as well as ambient room air that carries odors in wind tunnel (RA). The four-antenna array was then exposed to each of the four conditions until approximately 100 events had been detected for each condition. Every event was classified as A, B, AB, or RA.

unknown portion of the events in the training set contain events due to room air only. The classification scheme described here is a forced-choice algorithm, and with three training sets, any event will be classified as one of those three odors, even if the stimulus is actually a component of the background room air. By adding a fourth training set comprised of responses to room air (RA) only, it is more probable that RA will be correctly classified. The results of Figure 15.17 are typical when this technique is applied. It can be seen that odor A is correctly classified 95% of the time, odor B is correctly classified 83% of the time, and odor AB is correctly classified 64% of the time. Odor AB was a mixture of odor A and odor B, and while the pure mixture should give rise to a novel EAG response, the presumed classification mistakes occurring when odor AB was introduced were components odor A or odor B, as opposed to RA.

It is important to remember that each classification event takes less than 1 s. Unfortunately, even if the odors are highly distinguishable from RA, it is still possible for RA to be incorrectly classified as one of the training odors. One way to address this problem is to remove the clean-air events from the known odor training sets by reclassifying each training event as either clean air or the intended odor and then using these “verified” training data to classify unknown events. This represents just one possible refinement to this interesting pattern recognition problem.

## 15.9 FUTURE TRENDS

We have described the advantages, applications, technology, and methodology for incorporating a living olfactory organ into a hybrid-device biosensor. *Fast*, *sensitive*, and *discriminating* are all words that can be used to describe this sensor, but there is much yet to be done. Work is ongoing to refine the algorithm used to classify odors in order to increase accuracy. This includes the evaluation of features of the EAG signal other than peak amplitude and more robust pattern recognition strategies. Automating selection of thresholds and filter parameters and providing statistics describing the

confidence of a given classification are also being pursued. One fundamental challenge is the absence of a “gold standard” for odor strand composition under most field and laboratory conditions; that is, it is very difficult to know what the true odor is in a packet of air that elicits a response from the four-channel EAG biosensor. One method employed by Park et al. [22] was to bifurcate the air stream, passing half to an antenna and the other half to the flame ionization detector (FID) of a gas chromatograph. The arrival of a packet of air to each sensor (antenna and FID) was time locked, allowing unambiguous identification of the odor eliciting each antenna response. However, this arrangement is cumbersome and not easily translated to other settings.

Another aspect under development is the inclusion of wind direction and wind speed sensors. For an array of static sensors, for example, spaced 10 m apart along the edge of a field, wind information and triangulation can be used to locate the distant source of an odor. Incorporated into a single sensor, wind information could be used to guide a robotic mobile autonomous odor seeker (MAOS) in situations where approaching the odor source would present a high risk to people or trained dogs, for example, locating land mines or toxic chemical spills. Using Global Positioning System (GPS) technology, telemetry, and cameras, such a roving sensor could be deployed in military reconnaissance and search-and-rescue missions or to gather information near natural disaster areas. The extreme sensitivity could provide unexpected diagnostic benefits. The applications of olfactory biosensors are potentially quite broad, and it will likely be some time before artificial olfactory sensors can compare in performance. Perhaps the greatest limitation on this approach is the short-lived nature of the antennae (less than 1 h when removed from the insect); increasing the useful life of the hybrid sensor is also being pursued. Potential strategies include leaving the antenna attached to the insect, which increases the lifespan to several days, or using a supported olfactory receptor neuron culture system. The bioengineering challenges of this last approach are significant.

## REFERENCES

1. J. J. PANCRAZIO, J. P. WHELAN, D. A. BORHODER, W. MA, AND D. A. STENGER, Development and application of cell-based biosensors. *Ann. Biomed. Eng.* 27:697–711, 1999.
2. J. WHITE, T. A. DICKINSON, D. R. WALT, AND J. S. KAUER, An olfactory neuronal network for vapor recognition in an artificial nose. *Biol. Cybernet.* 78(4): 245–251, 1998.
3. S. E. STITZEL, L. J. COWEN, K. J. ALBERT, AND D. R. WALT, Array-to-array transfer of an artificial nose classifier. *Anal. Chem.* 73(21):5266–5271, 2001.
4. K. J. ALBERT, M. L. MYRICK, S. B. BROWN, D. L. JAMES, F. P. MILANOVICH, AND D. R. WALT, Field-deployable sniffer for 2,4-dinitrotoluene detection. *Environ. Sci. Technol.* 35(15):3193–3200, 2001.
5. T. A. DICKINSON, J. WHITE, J. S. KAUER, AND D. R. WALT, Current trends in “artificial-nose” technology. *TIBTECH* 16:250–258, 1998.
6. V. TORRE, J. F. ASHMORE, T. D. LAMB, AND A. MENINI, Transduction and adaptation in sensory receptor cells. *Review. J. Neurosci.* 15(12):7757–7768, 1995.
7. P. A. ANDERSON AND B. W. ACHE, Voltage- and current-clamp recordings of the receptor potential in olfactory receptor cells *in situ*. *Brain Res.* 338(2): 273–280, 1985.
8. T. V. GETCHELL, F. L. MARGOLIS, AND M. L. GETCHELL, Perireceptor and receptor events in vertebrate olfaction. *Review. Prog. Neurobiol.* 23(4): 317–345, 1984.
9. G. LAURENT, Olfactory network dynamics and the coding of multidimensional signals. *Nature* 3:884–895, 2002.
10. T. LILJEFORS, B. THELIN, AND J. N. C. VAN DER PERS, Structure-activity relationships between stimulus molecules and response of a pheromone receptor cell in turnip moth, *Agrotis segetum*: Modifications of the acetate group. *J. Chem. Ecol.* 10:1661–1675, 1984.
11. T. LILJEFORS, B. THELIN, J. N. C. VAN DER PERS, AND C. LÖFSTEDT, Chain-elongated analogues of a pheromone component of the turnip moth, *Agrotis segetum*. A structure-activity study using molecular mechanics. *J. Chem. Soc. Perkin Trans II*, 1957–1962, 1985.
12. T. LILJEFORS, M. BENGTTSSON, AND B. S. HANSSON, Effects of double-bond configuration on interaction between a moth sex pheromone component and its

- receptor: A receptor-interaction model based on molecular mechanics. *J. Chem. Ecol.* 13: 2023–2040, 1987.
13. T. C. BAKER AND K. F. HAYNES, Field and laboratory electroantennographic measurements of pheromone plume structure correlated with oriental fruit moth behaviour. *Physiol. Entomol.* 14:1–12, 1989.
  14. A. E. SAUER, G. KARG, U. T. KOCH, J. J. DE KRAMER, AND R. MILLI, A portable EAG system for the measurement of pheromone concentrations in the field. *Chem. Senses* 17:543–553, 1992.
  15. G. KARG AND A. E. SAUER, Spatial distribution of pheromone in vineyards treated for mating disruption of the grape vine moth *Lobesia botrana* measured with electroantennograms. *J. Chem. Ecol.* 21:1299–1314, 1995.
  16. J. N. C. VAN DER PERS AND A. K. MINKS, A portable electroantennogram sensor for routine measurements of pheromone concentrations in greenhouses. *Ent. Exp. Appl.* 87:209–215, 1998.
  17. K.-E. KAISLING, Insect olfaction. In *Handbook of Sensory Physiology*, Vol. 4, L. M. BEIDLER, Ed. Springer Verlag, Berlin, pp. 351–431, 1971.
  18. W. L. ROELOFS AND A. COMEAU, Sex pheromone perception: Electroantennogram responses of the red-banded leaf roller moth. *J. Insect Physiol.* 17:1969–1982, 1971.
  19. B. H. SMITH AND R. MENZEL, The use of electroantennogram recordings to quantify odourant discrimination in the honey bee, *Apis mellifera*. *J. Insect Physiol.* 35:369–375, 1989.
  20. J. H. VISSER, P. G. M. PIRON, AND J. HARDIE, The aphids' peripheral perception of plant volatiles. *Ent. Exp. Appl.* 80:35–38, 1996.
  21. J. H. VISSER AND P. G. M. PIRON, Olfactory antennal responses to plant volatiles in apterous virginoparae of the vetch aphid *Megoura viciae*. *Ent. Exp. Appl.* 77:37–46, 1997.
  22. K. C. PARK, S. A. OCHIENG, J. ZHU, AND T. C. BAKER, Odor discrimination using insect electroantennogram responses from an insect antennal array. *Chem. Senses* 27:343–352, 2002.
  23. D. R. WALT, T. DICKINSON, J. WHITE, J. KAURER, S. JOHNSON, H. ENGELHARDT, J. SUTTER, AND P. JURIS, Optical sensor arrays for odor recognition. *Biosens. Bioelectron.* 13:697–699, 1998.
  24. N. KASAI, I. SUGIMOTO, M. NAKAMURA, AND M. KATOH, Odorant detection capability of QCR sensors coated with plasma deposited organic films. *Biosens. Bioelectron.* 14:533–539, 1999.
  25. G. B. CLAYTON, *Operational Amplifiers*, 2nd ed. Butterworth, 1979.
  26. B. CLARK, Analog Devices Application Note 253, "Find Op Amp Noise with Spreadsheet," [http://www.analog.com/UploadedFiles/Application\\_Notes/353070850AN253.pdf](http://www.analog.com/UploadedFiles/Application_Notes/353070850AN253.pdf).

